Title

Wideband Planar Transmission Line Hyperbolic Metamaterial for Subwavelength Focusing and Resolution

Journal

IEEE Transactions on Microwave Theory and Techniques, 61(12)

ISSN

0018-9480

Authors

Sedighy, SH
Guclu, C
Campione, S
et al.

Publication Date

2013-11-22

DOI

10.1109/TMTT.2013.2288697

Peer reviewed

Wideband Planar Transmission Line Hyperbolic Metamaterial for Subwavelength Focusing and Resolution

S. Hassan Sedighy, Caner Guclu, *Student Member, IEEE*, Salvatore Campione, *Member, IEEE*, M. Khalaj Amirhosseini, and Filippo Capolino, *Senior Member, IEEE*

***Abstract*—We analyze both theoretically and experimentally subwavelength focusing by using a planar hyperbolic metamaterial (HM) at microwave frequencies. The proposed HM consists of microstrip transmission lines (TLs) loaded by lumped components and exhibits a very flat wave vector iso-frequency dispersion diagram over a wide frequency range, and thus able to transport spectral component with large wavenumbers. This flatness is here exploited to provide subwavelength focusing with a full width half maximum (3-dB power width) of about $\lambda_g/31$ and $\lambda_g/19$ at 0.5 and 1 GHz, respectively, where λ_g is the guided wavelength in the TL microtrip grid. Numerical simulation results are in good agreement with measurement ones. Moreover, we also investigate the capability of the proposed HM to resolve sources with subwavelength distance of about $\lambda_g/6$ and $\lambda_g/3$ at 0.5 and 1 GHz, respectively.**

***Index Terms*—Hyperbolic metamaterials (HMs), subwavelength focusing, subwavelength resolution, transmission lines (TLs).**

I. Introduction

THE resolution of a conventional lens is limited by the Abbe diffraction limit [1] that imposes a maximum resolution of $d = \lambda_0/(2n)$ with λ_0 the free-space wavelength and n the refractive index of the medium. This limitation rises from the fact that conventional lenses cannot transfer the evanescent spectrum emitted by a source, which is essential to reconstruct subwavelength information [2]. In other words, to overcome the diffraction limit one should transfer a very wide spatial spectrum of waves, including both propagating and evanescent components. The propagating (evanescent) spectrum includes all the spatial spectral components with transverse, to the lens axis, wavenumber k_t smaller (larger) than $k_0 n$, where $k_0 = 2\pi/\lambda_0$ is the free-space wavenumber.

Manuscript received March 07, 2013; revised October 10, 2013; accepted October 15, 2013. Date of publication November 14, 2013; date of current version December 02, 2013.

S. H. Sedighy is with the Department of Electrical Engineering and Computer Science, University of California at Irvine, Irvine, CA 92697 USA, and also with the School of New Technologies, Iran University of Science and Technology, Tehran 16846-13114, Iran.

C. Guclu, S. Campione, and F. Capolino are with the Department of Electrical Engineering and Computer Science, University of California at Irvine, Irvine, CA 92697 USA (e-mail: f.capolino@uci.edu).

M. K. Amirhosseini is with the Department of Electrical Engineering, Iran University of Science and Technology, Tehran 16846-13114, Iran.

Color versions of one or more of the figures in this paper are available online at http://ieeexplore.ieee.org.

Digital Object Identifier 10.1109/TMTT.2013.2288697

Transfer of both propagating and evanescent spectra has been achieved through the use of negative refractive index (NRI) materials. The "perfect lens" introduced by Pendry in [3] is a direct example of the fact that a slab of NRI material is able to *amplify* the evanescent spectral components emitted by a source, in addition to providing the standard focusing of the propagating spectrum. An NRI slab is thus able to compensate the evanescent decay in free space, overcoming the diffraction limit. However, the performance of a perfect lens is largely diminished by the presence of losses as outlined in [4] and [5]. Transmission line (TL) implementations of Pendry's lens have been reported in [6]–[9], where the NRI medium has been achieved via a periodically *LC*-loaded TL medium. The authors of [6]–[9] have demonstrated sub-diffraction focusing whose resolution limit is imposed by the periodicity of the implemented metamaterial NRI lens.

Another way of transferring both propagating and evanescent spectra is by using wire media [10]–[12], photonic crystals [13], and metal-dielectric multilayers [14]–[17] without involving the use of negative refraction or amplification of evanescent spectral components. All the artificial materials mentioned above support the propagation of a wide spatial spectrum of waves generated by one or more scatterers in their vicinity, otherwise evanescent in free space, due to the presence of a hyperbolic dispersion (see, e.g., [16] for more details). In the following, we refer to such artificial materials as hyperbolic metamaterials (HMs). It has been shown in [10], [13], [14], [17], and [18] that when these media possess a flat dispersion relation, in a regime referred to as *canalization regime*, they can be used to obtain subwavelength focusing. In other words, the canalization regime occurs when a wide spatial spectrum is allowed to propagate with almost the same phase constant inside the artificial medium. It is this peculiar regime that we are going to exploit in 2-D TL HM implementations for subwavelength focusing purposes. We note that, to the authors' knowledge, the use of very flat dispersion diagrams in 2-D TL HMs to achieve subwavelength focusing has not been demonstrated before.

As an alternative to the canalization regime investigated here, in the 2-D TL HM scenario, an *LC*-loaded TL grid capable of forming "resonance cones" [19], [20] has been experimentally demonstrated in [19] to achieve subwavelength focusing. Unloaded TL grids with unequal periods along the principal directions, creating anisotropy, have also been proven to support hyperbolic dispersion [21]. There, by interfacing two identical HMs, but one with 90° rotation, negative refraction and sub-

wavelength focusing have been achieved. In [22], the use of periodic circuits with unit cells comprising series capacitor or inductor in orthogonal directions led to extraordinary reflection and refraction phenomena including negative refraction.

Very recently, another experimental realization of HMs using 2-D TLs made of lumped capacitors and inductors has been reported in [23] with the goal of classifying the different configurations that lead to hyperbolic dispersion, however, without dealing with subwavelength focusing or with very flat dispersion.

In this paper, we utilize a planar 2-D TL HM with very flat dispersion that allows the subwavelength focusing by means of the above-mentioned canalization regime. The flatness of the HM dispersion curve is easy to design and realize experimentally in a 2-D TL grid, and this is a great motivation of our analysis. We thus demonstrate theoretically and experimentally the subwavelength focusing capabilities obtained by an HM with extremely flat dispersion diagram over a wide frequency range implemented by using loaded microstrip TLs. The wide frequency range of operation, without the change of focus location, constitutes the main advantage of the proposed design when compared to previous literature.

The outline of this paper is as follows. We construct in Section II the theoretical model required to calculate the wavenumber dispersion diagram in the planar HM implemented via TLs. We employ both Bloch theory and homogenization theory, and compare the two methods. The developed model is then adopted to design an HM with a very flat iso-frequency dispersion diagram used in the subsequent sections. The proposed finite structure with HM is simulated in Section III using a microwave circuit simulation package [Agilent Advanced Design System (ADS)], and it is shown to exhibit subwavelength focusing capabilities. We also show that the HM allows for the discrimination of two sources with subwavelength relative distance. In Section IV, we show the fabricated proposed HM design and experimental results exhibiting subwavelength focusing capabilities, in good agreement with simulation results. The required steps to achieve the iso-frequency dispersion diagrams according to both Bloch theory and homogenization theory are reported in Appendices A and B, respectively.

II. Hyperbolic Dispersion Diagrams in HMs Implemented via Planar TLs

A. Analytical Model

The 2-D microstrip TL grid implementation proposed here for subwavelength focusing and resolution is illustrated in Fig. 1. The upper 2-D "isotropic region," referred to as background medium [light blue in online version of Fig. 1(a) and (b)], is made by a 2-D microstrip TL grid with square unit cells. The lower HM region [light brown in online version of Fig. 1(a) and (b)] is realized by periodically loaded (by series lumped capacitors) microstrip lines, whose unit cell is shown in Fig. 1(c). In the following, we consider a square unit cell with period d along the x and z axes. The infinitely periodic representation of the HM design in Fig. 1(c) is studied here by using Bloch theory, following the formulation presented in [8]. The HM dispersion relation of the z-component of the

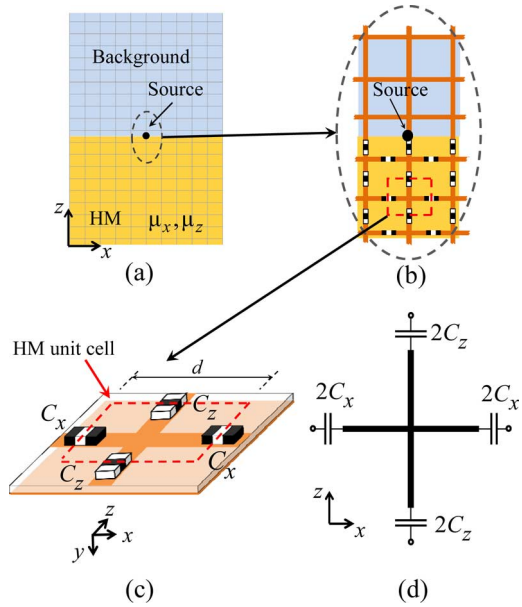

Fig. 1. (a) Schematic of the 2-D periodic TL implementation of HM. (b) Close-up view of the schematic in (a). (c) Illustration of the HM region unit cell. (d) Network representation of the HM region unit cell. Note that in the unit cell choice in (d), each microstrip segment is loaded by twice the capacitance in the relative direction.

wave vector k_z versus the x-component of the wave vector k_x is given by [see Appendix A for more details, where we assume a time harmonic convention of the kind $\exp(j\omega t)$]

$$\frac{\sin^2\left(\frac{k_z d}{2}\right)}{B^z} + \frac{\sin^2\left(\frac{k_x d}{2}\right)}{B^x} + j2Y_0 \sin\left(\frac{\beta d}{2}\right) = 0 \qquad (1)$$

where

$$B^{x,z} = jZ_0 \sin\left(\frac{\beta d}{2}\right) + \frac{1}{j2\omega C_{x,z}} \cos\left(\frac{\beta d}{2}\right). \qquad (2)$$

The coefficients $B^{x,z}$ are the "B" entries of the $ABCD$ matrices of the microstrip branches of length $d/2$ along the x and z axes in the unit cell that are loaded by capacitors $2C_x$ and $2C_z$, respectively, as illustrated in Fig. 1(d). Furthermore, $Z_0 = \sqrt{L_{\rm dis}/C_{\rm dis}}$ and $\beta = \omega\sqrt{L_{\rm dis}C_{\rm dis}}$ are the characteristic impedance and the propagation constant of the microstrip lines used in the grid implementation, respectively, where $L_{\rm dis}$ [H/m] and $C_{\rm dis}$ [F/m] are the distributed (per unit length) inductance and capacitance of the microstrip line (for simplicity, here we assume that TL segments along x and z are identical). As shown in Appendix B, in the particular case of the TL-grid period much smaller than the guided wavelength in the HM (i.e., $k_{x,z}d \ll 1$) and in the microstrip TL (i.e., $\beta d \ll 1$), the dispersion relation in (1) can be simplified to

$$\frac{k_z^2}{\mu_x} + \frac{k_x^2}{\mu_z} = \omega^2\varepsilon \qquad (3)$$

where

$$\mu_x = L_{\rm dis} - \frac{1}{\omega^2 C_z d} \quad \mu_z = L_{\rm dis} - \frac{1}{\omega^2 C_x d} \quad \varepsilon = 2C_{\rm dis}. \qquad (4)$$

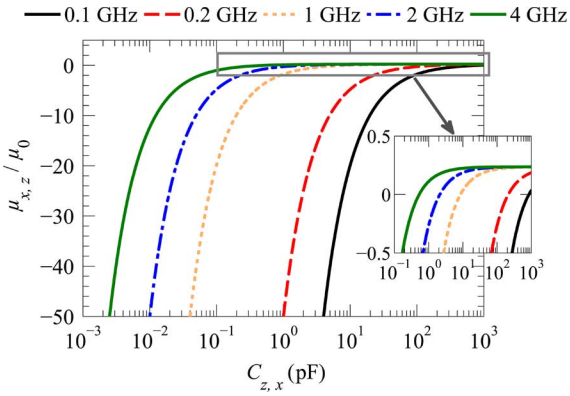

Fig. 2. (a) Relative permeability $\mu_{x,z}/\mu_0$ versus capacitance $C_{z,x}$ calculated by the homogenized medium approach (4) for various frequency values. The inset shows the region of small $\mu_{x,z}/\mu_0$ where zero crossing occurs.

Equation (3) is the wave vector dispersion relation in an effective homogeneous material with anisotropic (absolute) magnetic permeability represented by the tensor $\underline{\boldsymbol{\mu}} = \mu_x \hat{\mathbf{x}}\hat{\mathbf{x}} + \mu_z \hat{\mathbf{z}}\hat{\mathbf{z}}$ and the absolute effective permittivity ε. Based on (4), one can realize a positive μ_x and a negative μ_z or, vice versa, a positive μ_z and a negative μ_x, by proper loading the 2-D microstrip line with capacitors C_x and C_z. To show this feature, we plot the relative permeabilities $\mu_{x,z}/\mu_0$ versus $C_{z,x}$ in Fig. 2 (where μ_0 and ε_0 are the free-space absolute permeability and permittivity, respectively) for different frequencies, assuming 1.5-mm-wide microstrip lines on top of a grounded dielectric substrate (i.e., FR4) with relative permittivity $\varepsilon_{\rm FR4} = 4.5$ and thickness $h = 0.76$ mm, and square unit cells with $d = 1$ cm. This microstrip line is modeled by the distributed inductance $L_{\rm dis} = 298$ nH/m and capacitance $C_{\rm dis} = 127$ pF/m leading to the characteristic impedance $Z_0 = 48.4\ \Omega$. Under these assumptions, the background region (comprising the unloaded TL grid) corresponds to an effective isotropic medium with relative permeability $\mu_b/\mu_0 \approx 0.237$ and relative permittivity $\varepsilon_b/\varepsilon_0 \approx 28.7$ (where the subscript b stands for "background"). One can see from Fig. 2 that depending on the adopted capacitances $C_{z,x}$, the relative permeabilities $\mu_{x,z}/\mu_0$ cross zero for different capacitance values depending on the frequency. For any frequency, there is a capacitance value $C_{\rm res}$

$$C_{\rm res} = \frac{1}{\omega^2 L_{\rm dis} d} \tag{5}$$

responsible for a series resonance of the loaded microstrip branch (e.g., $C_{\rm res} = 8.5$ pF at 1 GHz). When $C_{z,x} < C_{\rm res}$ at a given frequency, the relative *permeability is negative* and has a steep behavior, i.e., it varies largely with small capacitance variations. On the contrary, for capacitance values $C_{z,x} > C_{\rm res}$, the relative permeability $\mu_{x,z}/\mu_0$ changes rather slowly and it approaches the unloaded microstrip line's permeability μ_b/μ_0 as $C_{z,x} \to \infty$, as the inset in Fig. 2 shows.

A hyperbolic dispersion diagram is obtained only when the ratio μ_z/μ_x is negative, as dictated by (3), i.e., when one of the two conditions is verified

$$C_x < C_{\rm res} < C_z \text{ or } C_z < C_{\rm res} < C_x \tag{6}$$

where the first or second condition corresponds to the HM with either μ_z or μ_x negative value. We continue with the condition

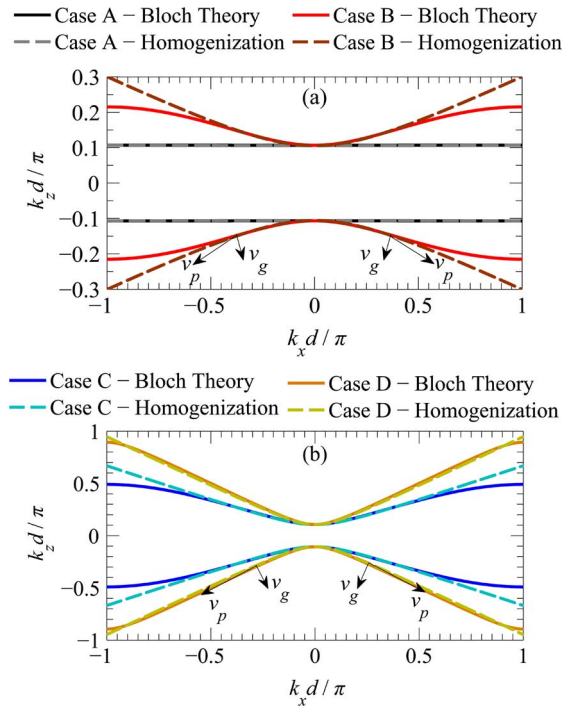

Fig. 3. $k_z - k_x$ wavenumber dispersion diagram at 1 GHz using Bloch theory (solid) and homogenization theory (dashed) of the 2-D TL HM for: (a) cases A and B and (b) cases C and D, described in Table I. The group and phase velocities are drawn to indicate the direction of power flow and phase propagation, respectively. The group velocity is along the frequency gradient of the dispersion surface so the Poynting vector is normal to the dispersion surface.

$C_x < C_{\rm res} < C_z$ (i.e., $\mu_z < 0, \mu_x > 0$) as it leads to a canalization regime. We also stress that the frequency band of canalization is intimately related to the chosen capacitance values: the low (high)-frequency edge is determined by $C_z(C_x)$ as for lower (higher) frequencies $C_{\rm res}$ increases (decreases) in view of (5). Thus, the condition $C_x < C_{\rm res} < C_z$ may be satisfied only for a wide, though limited frequency band. To outline a design procedure, we note that a large ratio μ_z/μ_x is determined by either having μ_z large or μ_x small, or both at the same time. We observe that a very small μ_x (governed by C_z) cannot be achieved in a wide frequency band. For this reason, we will assume in the experimental verification the condition $\mu_x \approx \mu_b$, realizable over a wide band, achieved with $C_z \to \infty$ (i.e., large), whereas μ_z large and negative can be easily achieved in a large frequency band by selecting a proper C_x, as will be illustrated next (for the sake of knowledge, we start by assuming a finite value for C_z).

By properly choosing the series loading capacitors for the HM TL region, we can then achieve different hyperbolic dispersion curves, including extremely flat ones. To stress this capability, in Fig. 3 we analyze the four representative cases of C_x summarized in Table I at 1 GHz under the assumption $C_z = 13.5$ pF ($\mu_x = 0.0877\ \mu_0$), considering that for these cases, $C_{\rm res} \approx 8.5$ pF.

In Fig. 3, we report the normalized dispersion diagrams by using (1) based on Bloch theory, and by using (3) based on homogenization theory. The plots show that the dispersion diagram evolves from a flat curve (Case A) to a steep hyperbola (Case D). In particular, Case A is characterized by a C_x

TABLE I
PERMEABILITY RATIOS FOR FOUR REPRESENTATIVE CASES OF CAPACITANCES C_x AT 1 GHz FOR THE HM UNDER INVESTIGATION WHEN $C_z = 13.5$ pF ($\mu_x = 0.0877\mu_0$)

Case	C_x	μ_z / μ_x
A	0.005 pF	−4600
B	1.5 pF	−12.6
C	4.6 pF	−2.30
D	6 pF	−1.13

smaller than the other cases, thus exhibiting a negative μ_z and $|\mu_z/\mu_x| \approx 4600$ much larger than the other three cases. Case D is instead characterized by a C_x larger than the other cases, still satisfying $C_x < C_{\rm res}$, and thus still exhibiting HM with a negative μ_z and $|\mu_z/\mu_x| \approx 1.13$, smaller than the other three cases. Accordingly, when keeping both C_z and frequency constant, a smaller C_x is required to achieve a very flat dispersion curve. In turn, the very flat dispersion curve assures that spatial spectral components with any k_x generated by a source at the interface of the HM region are able to propagate inside the HM with almost the same k_z, as can be ascertained by looking at Case A in Fig. 3 where for any k_x, $k_z d/\pi \approx 0.1$.

B. Proposed HM TL Design

Both background and HM TL grids are made here of 1.5-mm-wide microstrip lines above on a FR4 grounded dielectric substrate (the microstrip lines are as in Section II-A). The upper 12×23 unit cells represent the background medium and the bottom 11×23 unit cells represent the HM. The unit cell dimension is 1 cm × 1 cm ($0.0869\lambda_g \times 0.0869\lambda_g$), whereas the whole board size is 23 cm × 23 cm ($2\lambda_g \times 2\lambda_g$), where $\lambda_g = 11.5$ cm is the guided wavelength in the background medium at 1 GHz. The microstrip line segments are the same as in Section II-A, thus modeled by the same $L_{\rm dis}$ and $C_{\rm dis}$ values provided there. The microstrips in the HM region are loaded in series with capacitances for achieving here a very flat dispersion curve.

Consider now Case A in Table I ($C_x = 0.005$ pF) that exhibits a very flat dispersion diagram, as reported in Fig. 3. It can be inferred from Fig. 2 that μ_x/μ_0 varies from 0.0877 to 0.237 when C_z is increased from 13.5 pF to infinity (short circuit). Also, replacing the capacitor C_z with a short circuit decreases the ratio $|\mu_z/\mu_x|$ from 4600 to 1700 at 1 GHz and this change implies a slightly less flat dispersion diagram, though still much flatter than the other three cases in Table I. Therefore, for simplicity of realization, we show that if we increase C_z from 13.5 pF to infinity, the $k_z - k_x$ dispersion curves remain still very flat, as reported in Fig. 4 (obtained by Bloch theory) at 1 GHz. Note that k_z varies due to the change in μ_x/μ_0; in particular, $k_z d/\pi$ goes from 0.1 to about 0.2. This is still good for the purpose of employing the canalization regime, and the choice of $C_z \to \infty$ (short circuit) eases the fabrication realization. Regarding C_x, instead, we keep the one reported in Table I for Case A ($C_x = 0.005$ pF), which is realized simply by a 1-mm gap in the x-directed TL branches (the value of this gap capacitance has been verified by using the finite-element method full-wave solver HFSS by Ansys Inc.). We further show that this

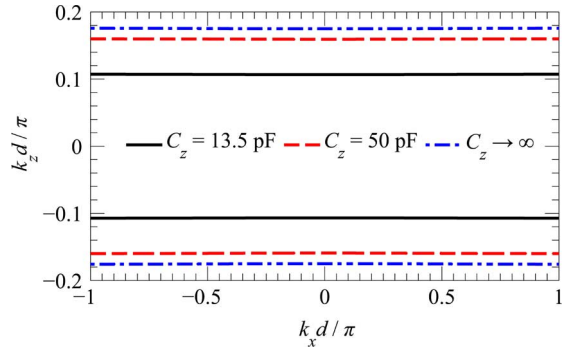

Fig. 4. $k_z - k_x$ wavenumber dispersion diagram obtained by Bloch theory for the 2-D TL HM medium versus lumped capacitance C_z. Other design parameters are as in Case A in Fig. 3.

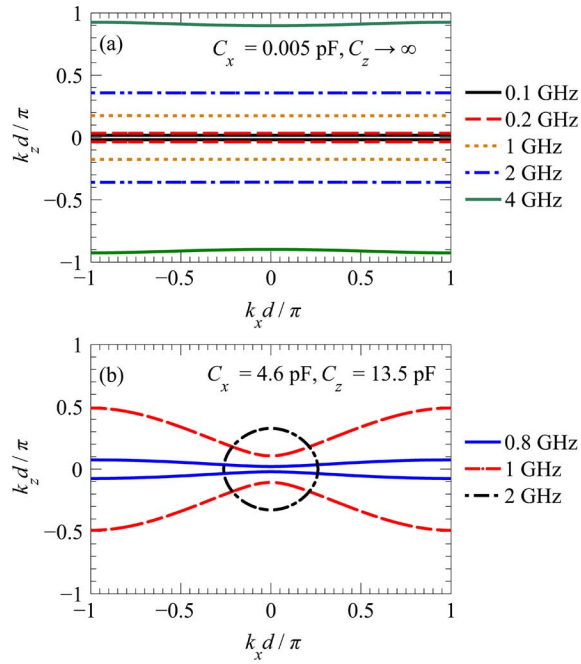

Fig. 5. $k_z - k_x$ wavenumber dispersion diagram obtained by Bloch theory for the 2-D TL HM medium for various representative frequencies for: (a) Case A in Fig. 3, using $C_z \to \infty$ (i.e., short circuit) and (b) Case C. Note that, in (a), the curves remain flat for a wide frequency range, whereas in (b), the hyperbolic dispersion varies considerably with frequency and is even lost, becoming elliptic, for instance, at 2 GHz.

design is characterized by a very flat dispersion diagram for a wide frequency band (0.1–4 GHz), as reported in Fig. 5(a) (obtained by Bloch theory), where only the propagating k_z value varies from case to case. The obtained very flat iso-frequency dispersion diagrams imply that the reported 2-D TL HM can be in principle used for subwavelength focusing applications with large bandwidth of operation. In contrast, we show in Fig. 5(b) the dispersion diagram at various frequencies for Case C. Below 0.8 GHz, both μ_x and μ_z are negative for Case C, implying that the 2-D TL grid hosts only evanescent waves. However, above 0.8 GHz we observe hyperbolic dispersion because μ_x becomes positive. As the frequency increase, μ_z also turns positive, and thus, the hyperbolic dispersion is lost as depicted by the dotted–dashed black elliptic curve at 2 GHz in Fig. 5(b). This strengthens our choice of the flat dispersion for which we have a wider frequency band of operation.

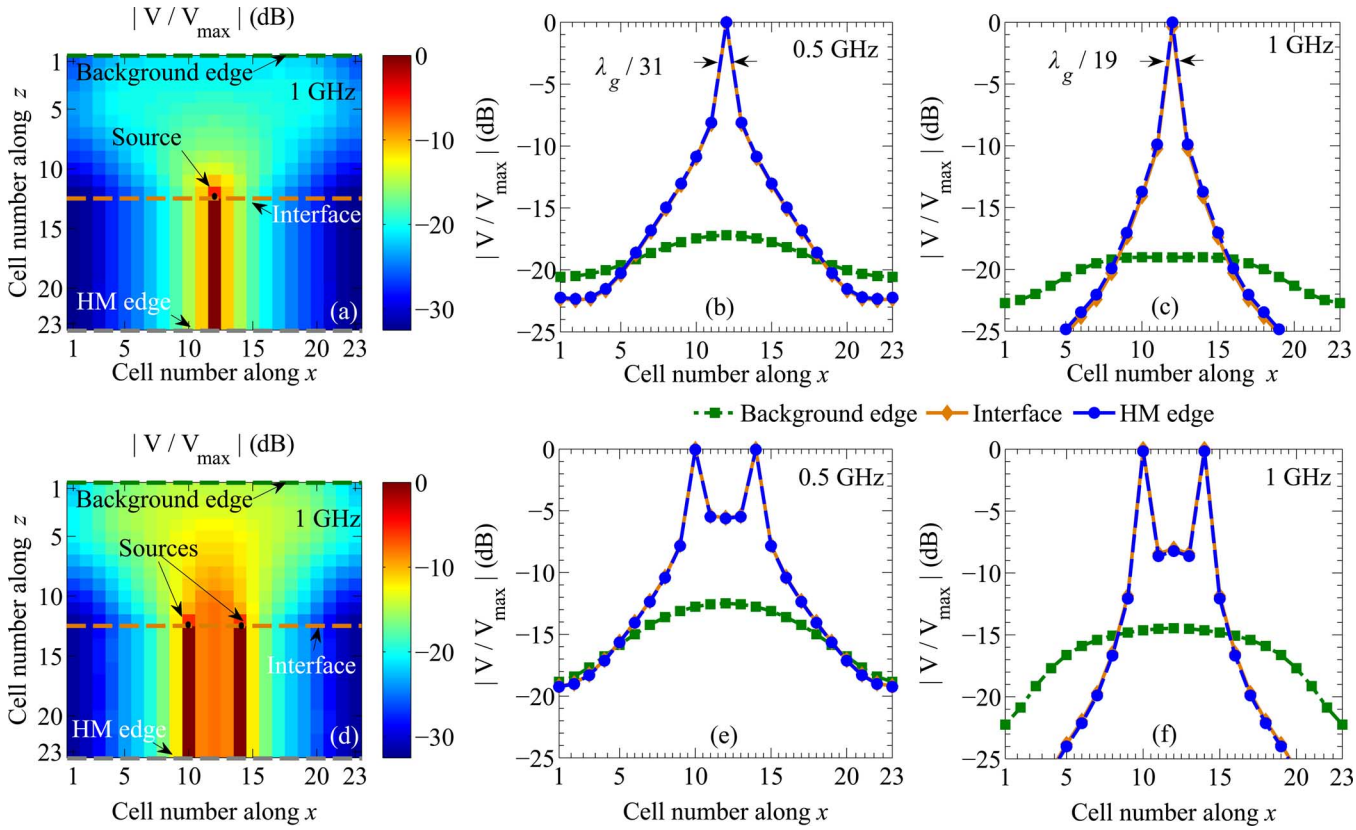

Fig. 6. Simulated voltage magnitude distribution, normalized by the maximum voltage $V_{\max}$ on the designed board, at 1 GHz for: (a) one and (d) two excitation point sources. Normalized voltage magnitude at the interface, top, and bottom edges of the structure for: (b) one point source at 0.5 GHz, (c) one point source at 1 GHz, (e) two point sources at 0.5 GHz, and (f) two point sources at 1 GHz.

C. Evaluation of TL Termination Impedances via Bloch Theory

Due to the finite size of the designed board, the reflection from the board edges should be avoided in order to mimic semi-infinite HM and background half-spaces. For this reason, the TL grids (for both background and HM) need to be terminated to proper impedances. Here, similarly to what done in [8], the proper termination impedances are equal to the Bloch impedances

$$Z_{x,z} = \frac{Z_0 \tan(\beta d/2) - \frac{1}{2\omega C_{x,z}}}{\tan(k_{x,z} d/2)} \tag{7}$$

where the subscripts x and z of Z indicate the direction of the termination (i.e., Z_x is the Bloch impedance for terminating the TLs along the x direction).

As discussed in Section II-B, because of the flat dispersion diagram, all the spectral waves in the HM propagate with almost the same wavenumber along the z direction as $k_z = \omega\sqrt{\mu_x \varepsilon}$. By using (7) and the TL parameters introduced in the previous sections, the HM Bloch termination is 33 Ω, which matches waves propagating along the $-z$ direction. Note that since the power inside the HM is canalized mainly into the $-z$ direction, the power propagating in the $+$ or $-$ x directions is negligible; hence, we can leave the TL endings along x as open circuit. For the background medium, that is characterized by a circular iso-frequency dispersion wavenumber curve, the Bloch impedances in the x and z directions vary for any wavenumber pair (k_x, k_z), i.e., with the angle of propagation. Based on the background medium dimensions, the waves excited at the center of the board, that are, in turn, incident on the three edges of the upper background region in Fig. 1, have an angle of incidence between 0° and 45°. This means that the ratio $k_{x,z}/k_b$, with $k_b = \omega\sqrt{\mu_b \varepsilon_b} = \omega\sqrt{L_{\rm dis} 2C_{\rm dis}}$, changes between 0 and $1/\sqrt{2}$. Thus, using (7) and the TL parameters from the previous section, the Bloch impedances in the z and x directions change from a minimum of 29 Ω for $k_{x,z}/k_b = 0$ to a maximum of 42 Ω for $k_{x,z}/k_b = 1/\sqrt{2}$. For simplicity, we chose to terminate all TLs in the background part with a constant resistance of 33 Ω. A detailed analysis of this choice has been carried out proving that this constant termination impedance causes negligible reflection from the boundaries (not reported here for brevity) and this does not hinder the subwavelength focusing capabilities.

III. Numerical Simulations of Subwavelength Focusing and Resolution

We use a microwave circuit simulator (Agilent Technologies' ADS) to simulate the design discussed in Sections II-B and II-C. A shunt voltage source is exerted between the ground and the TL grid at the center of the interface between the background and the HM, as illustrated in Fig. 1(b). The voltage of the nodes (intersection points of microstrip lines along x and z) toward the ground, in the case of a single voltage source excitation at 1 GHz, is shown in Fig. 6(a). The color of each square represents the node voltage (in decibels) of the board normalized with respect to the maximum voltage in the board, which occurs to be the voltage of the closest node to the source on the HM side. The canalization regime is clearly observed in Fig. 6(a). We also report the normalized node voltages versus the cell number along x, at the

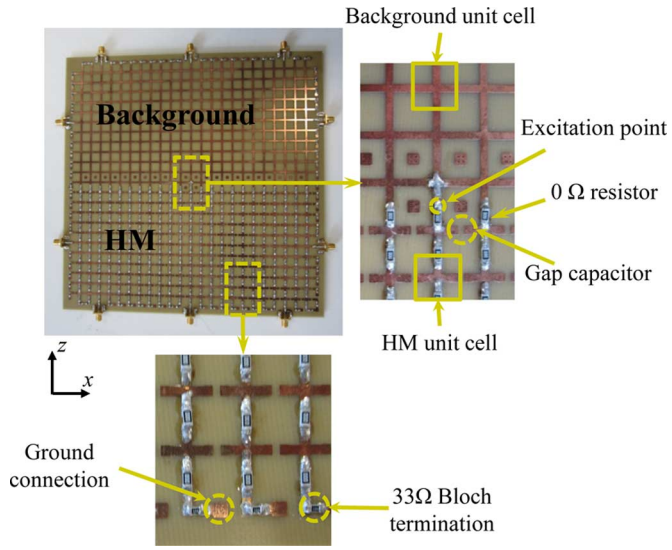

Fig. 7. Fabricated TL grid over a grounded dielectric substrate. The background and HM are represented by the upper and lower half parts of the TL grid, respectively. Each component is indicated by yellow lines (in the online version).

interface between the HM and the background, at the top (background) edge, and at the bottom (HM) edge in Fig. 6(b) and (c), at 0.5 and 1 GHz, respectively. These plots show that the voltage profile along the HM-background interface is transferred to the bottom edge of the HM region with almost the same pattern, indicating that the HM is able to transport all the large wavenumber spectral components generated by the voltage source. Instead, the voltage profile at the top edge of the background region (the isotropic region) shows that focusing is lost because waves with large spectral wavenumbers are evanescent and thus do not propagate away from the source. In summary, the source information in free space is lost due to evanescent decay, whereas it is kept in the HM because waves with large wavenumbers are propagating in the HM. We annotate the full width half maximum (FWHM) by arrows and the result in Fig. 6(b) and (c) clearly shows that subwavelength focusing with FWHM of $\lambda_g/31$ and $\lambda_g/19$ at 0.5 and 1 GHz is achieved, respectively.

Next, we consider the case of two point sources with subwavelength distance of 4 cm (equal to $\lambda_g/6$ and $\lambda_g/3$ at 0.5 and 1 GHz, respectively) to verify the potential of subwavelength resolution. Fig. 6(d) shows the voltage color map of the case with two voltage sources, and we show that the voltage of each source is clearly canalized in the HM. Moreover the normalized voltage profiles at the interface, top edge of the background medium, and bottom edge of the HM media are reported in Fig. 6(e) and (f), at 0.5 and 1 GHz, respectively. It can be seen that the peaks of the two sources are clearly resolved and a resolution of sources with an inter-distance of at least $\lambda_g/6$ at 0.5 GHz and $\lambda_g/3$ at 1 GHz is achieved.

IV. Measurement Results of Subwavelength Focusing

In this section, we elaborate on the fabrication and measurement of the design whose specifications and simulation results were provided in Sections II and III. For implementation purposes, we used a TL grid printed with placement pads left for surface mounted devices (SMDs). The fabricated circuit board

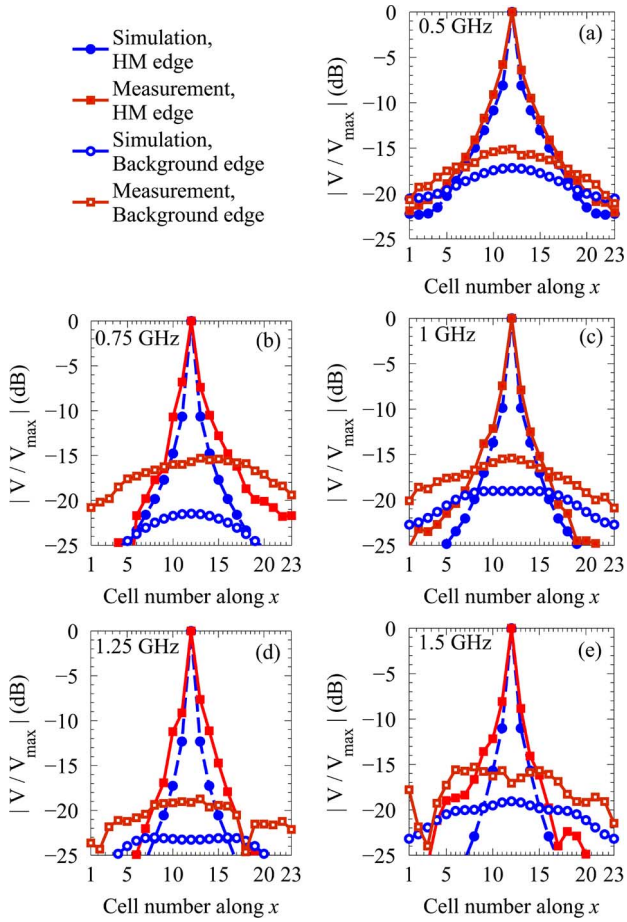

Fig. 8. Simulation and measurement results of the voltage magnitude profile at the HM bottom edge and at the background top edge normalized by the maxima $V_{\max}$ at the HM bottom edge for simulation and measurements respectively at 0.5, 0.75, 1, 1.25, and 1.5 GHz. Measured and simulated results, in good agreement, show that subwavelength focusing is preserved across the HM.

with FR4 grounded dielectric substrate is depicted in Fig. 7. We used 0-Ω SMD resistors in the z direction for realization of $C_z \rightarrow \infty$, whereas the microstrip gap capacitance on the SMD placement pads were sufficient along the x direction to achieve the designed capacitance value of $C_x = 0.005$ pF in Case A in Table I and Fig. 5 (designed to achieve a very flat wavenumber dispersion diagram). At the center of the board, an SMA connector is mounted from the bottom side and is connected to one port of the vector network analyzer (VNA) (Rhode Schwarz ZVA67). The second port of the VNA is connected to an in-house built probe (which is a modified SMA edge-mount connector with two points of contact, one for ground and one for signal to ensure low-resistance contacts across the termination resistors). S_{21} is then recorded along the HM (bottom) and the background (top) edges by sampling S_{21} for each termination resistor. Note that all the termination resistors have the same value of 33 Ω, therefore S_{21} values are indicative of the voltage along the edges. We first start discussing the measurement across the bottom edge of the HM. Simulation have been carried out in order to assure that the probe impedance (as a parallel 50 Ω to the termination impedance) does not have a significant impact on the results and this method is sufficiently accurate for the purpose of showing subwavelength focusing. Fig. 8 shows the measurement and simulated voltage profiles

(normalized to the maximum value at the HM bottom edge) at the HM bottom edge of the structure at 0.5, 0.75, 1, 1.25, and 1.5 GHz, respectively. It is clear that the voltage profile at the bottom edge of the HM is almost a replica of the voltage profile along the x direction at the interface between the two grid media, therefore exhibiting a focus with subwavelength dimension. Similar to what was done for the HM bottom edge, we have also reported the simulation and experimental results relative to a scan line at the background top edge. The presence of a very flat voltage profile shows that focusing is lost, as expected, due to evanescent decay of the large spectral component in the isotropic region (i.e., the background grid) generated by the voltage source. The small disagreement, in -15- to -20-dB range, may be due to the nonperfect contact between the probe and the metallization on the circuit board, to the 5%–10% tolerance in termination resistances, and to the probe loading the termination resistors (in particular, the latter might affect the recorded signal along HM and background edges differently). In summary, after comparing the voltage profiles along the HM bottom and background top edges, these results numerically and experimentally verify the subwavelength focusing capabilities of the proposed HM-based device over a wide frequency band.

V. Conclusion

This paper has shown a practical implementation of a planar (2-D) HM able to transport waves with a large spectral wavenumber. In particular, the planar HM is realized using microstrip TLs, and is designed to achieve subwavelength focusing over a wide frequency range by engineering very flat and stable-with-frequency wavenumber hyperbolic dispersion curves. This has been achieved by loading a TL grid with capacitors in the x and z directions, leading to a canalization regime for the node voltage in the HM region. We have shown that the HM design can provide subwavelength focusing of $\lambda_g/31$ and $\lambda_g/19$ at 0.5 and 1 GHz, respectively, with good agreement between simulation and measurement results. We have also shown that the proposed HM can be used to resolve two sources separated by subwavelength distance of $\lambda_g/6$ and $\lambda_g/3$ at 0.5 and 1 GHz, respectively.

Appendix A
Derivation of the Dispersion Relation via Bloch Theory

According to Bloch theory applied to 2-D TLs [8], the wavevector dispersion relation of a loaded 2-D TL grid is obtained by solving the equation

$$B^x D^x[\cos(k_z d) - (C^z B^z + A^z D^z)] + B^z D^z[\cos(k_x d) - (C^x B^x + A^x D^x)] = 0 \quad (8)$$

where

$$A^{x,z} = \cos\left(\frac{\beta d}{2}\right) + \frac{1}{Z_0 \omega 2C_{x,z}} \sin\left(\frac{\beta d}{2}\right) \quad (9)$$

$$B^{x,z} = jZ_0 \sin\left(\frac{\beta d}{2}\right) + \frac{1}{j\omega 2C_{x,z}} \cos\left(\frac{\beta d}{2}\right) \quad (10)$$

$$C^{x,z} = jY_0 \sin\left(\frac{\beta d}{2}\right) \quad (11)$$

$$D^{x,z} = \cos\left(\frac{\beta d}{2}\right) \quad (12)$$

are the transfer ($ABCD$) matrix entries of the microstrip lines of length $d/2$ (with characteristic impedance $Z_0 = 1/Y_0$ and wavenumber β) along the x and z axes (indicated by the superscripts x and z) loaded by capacitors $2C_{x,z}$ in a $d \times d$ unit cell, as depicted in Fig. 1(d). Due to the reciprocity of the unit cell, it follows that $A^{x,z}D^{x,z} - B^{x,z}C^{x,z} = 1$, thus,

$$B^x D^x[\cos(k_z d) - (2C^z B^z + 1)] + B^z D^z[\cos(k_x d) - (2C^x B^x + 1)] = 0. \quad (13)$$

Moreover, due to the symmetry of the unit cell in our setup, $C^z = C^x$ and $D^z = D^x$, thus the dispersion relation can be further simplified as

$$B^x\left[\sin^2\left(\frac{k_z d}{2}\right) + C^x B^z\right] + B^z\left[\sin^2\left(\frac{k_x d}{2}\right) + C^x B^x\right] = 0. \quad (14)$$

By dividing all the terms in (14) by $B^x B^z$ and substituting C^x from (11), we arrive at the dispersion relation in (1).

Appendix B
Effective Medium Approach as a Particular Case of Bloch Theory

It is interesting how the effective medium model can be derived from the Bloch formulation based on the transfer matrix approach. We can simplify the dispersion relation in (1) by assuming $k_{x,z}d \ll 1$ and $\beta d \ll 1$. After using the approximation $\sin(k_{x,z}d/2) \approx k_{x,z}d/2$, (1) is rewritten as

$$\frac{\left(\frac{k_z d}{2}\right)^2}{B^z} + \frac{\left(\frac{k_x d}{2}\right)^2}{B^x} = -j2Y_0 \sin\left(\frac{\beta d}{2}\right). \quad (15)$$

By using the approximations $\sin(\beta d/2) \approx \beta d/2$ and $\cos(\beta d/2) \approx 1$, the expressions $B^{x,z}$ [given in (2)] are then simplified as

$$B_{x,z} \approx jZ_0 \frac{\beta d}{2} + \frac{1}{2j\omega C_{x,z}}. \quad (16)$$

The right-hand side of (15) is also simplified as

$$-j2Y \sin\left(\frac{\beta d}{2}\right) \approx -jY_0 \beta d. \quad (17)$$

By replacing approximations (16) and (17) into (15) and using the definitions $\beta = \omega\sqrt{L_{\rm dis}C_{\rm dis}}$ and $Z_0 = \sqrt{L_{\rm dis}/C_{\rm dis}}$, we reach the dispersion relation of the HM effective medium approach as given in (3).

Note that for the background isotropic region, where we can assume $C_{x,z} = \infty$, the dispersion relation (3) leads to the wavenumber in the background region $k_b = \sqrt{k_x^2 + k_z^2} = \omega\sqrt{\mu_b \varepsilon_b} = \omega\sqrt{L_{\rm dis}2C_{\rm dis}} = \beta\sqrt{2}$, where $\mu_b = \mu_x = \mu_z = L_{\rm dis}$ and $\varepsilon_b = 2C_{\rm dis}$.

ACKNOWLEDGMENT

The authors are thankful to Rhode Schwarz for the measurement equipment, to Ansys Inc. for providing HFSS, and to Agilent Technologies for providing ADS, instrumental in the present analysis. The authors thank K. Rice, S. Park, and K. Vuong, all with the University of California at Irvine, Irvine, CA, USA, for their contribution to the experimental setup.

REFERENCES

[1] M. Born and E. Wolf, *Principles of Optics*, 7th ed. Cambridge, U.K.: Cambridge Univ. Press, 1999.

[2] P. A. Belov and M. G. Silveirinha, "Resolution of subwavelength transmission devices formed by a wire medium," *Phys. Rev. E, Stat. Phys. Plasmas Fluids Relat. Interdiscip. Top.*, vol. 73, May 2006, Art. ID 056607.

[3] J. B. Pendry, "Negative refraction makes a perfect lens," *Phys. Rev. Lett.*, vol. 85, pp. 3966–3969, Oct. 2000.

[4] D. R. Smith, D. Schurig, M. Rosenbluth, S. Schultz, S. A. Ramakrishna, and J. B. Pendry, "Limitations on subdiffraction imaging with a negative refractive index slab," *Appl. Phys. Lett.*, vol. 82, pp. 1506–1508, Mar. 2003.

[5] D. Maystre and S. Enoch, "Perfect lenses made with left-handed materials: Alice's mirror?," *J. Opt. Soc. Amer. A, Opt. Image Sci.*, vol. 21, pp. 122–131, Jan. 2004.

[6] A. Grbic and G. V. Eleftheriades, "Negative refraction, growing evanescent waves, and sub-diffraction imaging in loaded transmission-line metamaterials," *IEEE Trans. Microw. Theory Techn.*, vol. 51, no. 12, pp. 2297–2305, Dec. 2003.

[7] A. Grbic and G. V. Eleftheriades, "Growing evanescent waves in negative-refractive-index transmission-line media," *Appl. Phys. Lett.*, vol. 82, pp. 1815–1817, Mar. 2003.

[8] A. Grbic and G. V. Eleftheriades, "Periodic analysis of a 2-D negative refractive index transmission line structure," *IEEE Trans. Antennas Propag.*, vol. 51, no. 10, pp. 2604–2611, Oct. 2003.

[9] A. K. Iyer, P. C. Kremer, and G. V. Eleftheriades, "Experimental and theoretical verification of focusing in a large, periodically loaded transmission line negative refractive index metamaterial," *Opt. Exp.*, vol. 11, pp. 696–708, Apr. 2003.

[10] P. A. Belov, Y. Hao, and S. Sudhakaran, "Subwavelength microwave imaging using an array of parallel conducting wires as a lens," *Phys. Rev. B, Condens. Matter*, vol. 73, Jan. 2006, Art. ID 033108.

[11] X. Radu, A. Lapeyronnie, and C. Craeye, "Numerical and experimental analysis of a wire medium collimator for magnetic resonance imaging," *Electromagnetics*, vol. 28, pp. 531–543, Sep. 2008.

[12] X. Radu, D. Garray, and C. Craeye, "Toward a wire medium endoscope for MRI imaging," *Metamaterials*, vol. 3, pp. 90–99, Oct. 2009.

[13] P. A. Belov, C. R. Simovski, and P. Ikonen, "Canalization of subwavelength images by electromagnetic crystals," *Phys. Rev. B, Condens. Matter*, vol. 71, May 2005, Art. ID 193105.

[14] Y. Jin, "Improving subwavelenght resolution of multilayered structures containing negative-permittivity layers by flatting the transmission curves," *PIER*, vol. 105, pp. 347–364, 2010.

[15] D. R. Smith and D. Schurig, "Electromagnetic wave propagation in media with indefinite permittivity and permeability tensors," *Phys. Rev. Lett.*, vol. 90, Feb. 2003, Art. ID 077405.

[16] C. Guclu, S. Campione, and F. Capolino, "Hyperbolic metamaterial as super absorber for scattered fields generated at its surface," *Phys. Rev. B, Condens. Matter*, vol. 86, Nov. 2012, Art. ID 205130.

[17] P. A. Belov and Y. Hao, "Subwavelength imaging at optical frequencies using a transmission device formed by a periodic layered metal-dielectric structure operating in the canalization regime," *Phys. Rev. B, Condens. Matter*, vol. 73, Mar. 2006, Art. ID 113110.

[18] W. Yan, N. A. Mortensen, and M. Wubs, "Hyperbolic metamaterial lens with hydrodynamic nonlocal response," *Opt. Exp.*, vol. 21, pp. 15026–15036, Jun. 2013.

[19] K. G. Balmain, A. A. E. Luttgen, and P. C. Kremer, "Resonance cone formation, reflection, refraction, and focusing in a planar anisotropic metamaterial," *IEEE Antennas Wireless Propag. Lett.*, vol. 1, pp. 146–149, Nov. 2002.

[20] J. K. H. Wong, K. G. Balmain, and G. V. Eleftheriades, "Fields in planar anisotropic transmission-line metamaterials," *IEEE Trans. Antennas Propag.*, vol. 54, no. 10, pp. 2742–2749, Oct. 2006.

[21] G. V. Eleftheriades and O. F. Siddiqui, "Negative refraction and focusing in hyperbolic transmission-line periodic grids," *IEEE Trans. Microw. Theory Techn.*, vol. 53, no. 1, pp. 396–403, Jan. 2005.

[22] Y. Feng, X. Teng, Y. Chen, and T. Jiang, "Electromagnetic wave propagation in anisotropic metamaterials created by a set of periodic inductor-capacitor circuit networks," *Phys. Rev. B, Condens. Matter*, vol. 72, Dec. 2005, Art. ID 245107.

[23] P. V. K. Alyona, V. Chshelokova, A. N. Poddubny, D. S. Filonov, A. P. Slobozhanyuk, Y. S. Kivshar, and P. A. Belov, "Hyperbolic transmission-line metamaterials," *J. Appl. Phys.*, vol. 112, Oct. 2012, Art. ID 073116.

S. Hassan Sedighy, photograph and biography not available at time of publication.

Caner Guclu (S'10), photograph and biography not available at time of publication.

Salvatore Campione (S'08–M'09), photograph and biography not available at time of publication.

M. Khalaj Amirhosseini, photograph and biography not available at time of publication.

Filippo Capolino (S'95–M'97–SM'04), photograph and biography not available at time of publication.